

Contact inhibition of locomotion and mechanical cross-talk between cell–cell and cell–substrate adhesion determine the pattern of junctional tension in epithelial cell aggregates

Luke Coburn^{a,b,*}, Hender Lopez^{a,c}, Benjamin J. Caldwell^d, Elliott Moussa^d, Chloe Yap^d, Rashmi Priya^d, Adrian Noppe^e, Anthony P. Roberts^e, Vladimir Lobaskin^a, Alpha S. Yap^d, Zoltan Neufeld^{d,e}, and Guillermo A. Gomez^{d,*}

^aSchool of Physics and Complex and Adaptive Systems Laboratory, University College Dublin, Belfield, Dublin 4, Ireland; ^bInstitute of Complex Systems and Mathematical Biology, University of Aberdeen, Aberdeen AB24 3FX, United Kingdom; ^cCenter for BioNano Interactions, School of Chemistry and Chemical Biology, University College Dublin, Belfield, Dublin 4, Ireland; ^dInstitute for Molecular Bioscience, Division of Cell Biology and Molecular Medicine, and ^eSchool of Mathematics and Physics, University of Queensland, St. Lucia, Brisbane 4072, Australia

ABSTRACT We used a computational approach to analyze the biomechanics of epithelial cell aggregates—islands, stripes, or entire monolayers—that combines both vertex and contact-inhibition-of-locomotion models to include cell–cell and cell–substrate adhesion. Examination of the distribution of cell protrusions (adhesion to the substrate) in the model predicted high-order profiles of cell organization that agree with those previously seen experimentally. Cells acquired an asymmetric distribution of basal protrusions, traction forces, and apical aspect ratios that decreased when moving from the edge to the island center. Our *in silico* analysis also showed that tension on cell–cell junctions and apical stress is not homogeneous across the island. Instead, these parameters are higher at the island center and scale up with island size, which we confirmed experimentally using laser ablation assays and immunofluorescence. Without formally being a three-dimensional model, our approach has the minimal elements necessary to reproduce the distribution of cellular forces and mechanical cross-talk, as well as the distribution of principal stress in cells within epithelial cell aggregates. By making experimentally testable predictions, our approach can aid in mechanical analysis of epithelial tissues, especially when local changes in cell–cell and/or cell–substrate adhesion drive collective cell behavior.

Monitoring Editor

Manuel Théry
CEA, Hopital Saint Louis

Received: Apr 12, 2016
Revised: Aug 23, 2016
Accepted: Aug 30, 2016

INTRODUCTION

In epithelial tissues, the capacity of epithelial cells to alter their shape, move, and exchange neighbors is profoundly influenced by the biochemical and mechanical properties of the tissue (Mammoto

et al., 2013; Lecuit and Yap, 2015; Mao and Baum, 2015). Adhesion, either to the substrate or to another cell, allows cells to probe and respond to the mechanical properties of their environment. At the sites of cell–cell junctions, adhesion receptors such as cadherins couple the contractile actomyosin apparatus of epithelial cells together to generate junctional tension (Gomez et al., 2011). Physical tension on junctions has been revealed by a variety of methods, including laser ablation (Ratheesh et al., 2012; Smutny et al., 2015), optical tweezers (Bambardekar et al., 2015), fluorescence resonance energy transfer (FRET) tension sensors (Grashoff et al., 2010; Borghi et al., 2012; Conway et al., 2013; Leerberg et al., 2014), and immunofluorescence for protein epitopes that are revealed under tension (Yonemura et al., 2010). In particular, FRET-based molecular tension sensors have been useful to show that both E-cadherin and vinculin molecules experience tension when localized at the epithelial cell

This article was published online ahead of print in MBoC in Press (<http://www.molbiolcell.org/cgi/doi/10.1091/mbc.E16-04-0226>) on September 7, 2016.

*Address correspondence to: Luke Coburn (lukecoburn@gmail.com), Guillermo A. Gomez (g.gomez@uq.edu.au).

Abbreviations used: CIL, contact inhibition of locomotion; MCS, Monte Carlo step; TFM, traction force microscopy.

© 2016 Coburn et al. This article is distributed by The American Society for Cell Biology under license from the author(s). Two months after publication it is available to the public under an Attribution–Noncommercial–Share Alike 3.0 Unported Creative Commons License (<http://creativecommons.org/licenses/by-nc-sa/3.0/>).

"ASCB®," "The American Society for Cell Biology®," and "Molecular Biology of the Cell®" are registered trademarks of The American Society for Cell Biology.

junctions (Borghetti et al., 2012; Leerberg et al., 2014). At the cell–substrate interface, integrin receptors interact with ligands in the extracellular matrix and exert forces on these adhesion sites, probing the mechanical properties of the substrate. This process allows maturation and recruitment of signaling and adaptor proteins to these adhesion sites (Grashoff et al., 2010; Roca-Cusachs et al., 2013).

Traction force microscopy (TFM) has been instrumental in measuring the direction and magnitude of forces that cells apply on their substrate (Saez et al., 2010; Style et al., 2014; Martiel et al., 2015). When applied to clusters of epithelial cells and combined with Newton's law of force balance, this technique also allows the inferred measurement of “tugging” forces that occur on cell–cell junctions and the physical stress in the monolayer (Trepaut et al., 2009; Liu et al., 2010; Maruthamuthu et al., 2011; Tambe et al., 2013; Ng et al., 2014). In the case of a pair of cells, traction forces develop principally at the periphery of the cell cluster and are balanced with tugging forces exerted by cells at their cell–cell junctions (Liu et al., 2010; Maruthamuthu et al., 2011). Bigger cell clusters (>2–1000 cells) still show some similarities with a pair of cells, with traction forces localized primarily at the periphery of the cluster (Trepaut et al., 2009; Mertz et al., 2013; Ng et al., 2014). However, under these circumstances, traction forces also develop in cells behind the border or leader cells that are located at the edges of the cluster, as these cells are able to form cryptic lamellipodia that extend underneath their neighbors (Trepaut et al., 2009). Videomicroscopy, on the other hand, has shown that higher velocities exhibited by leader cells at the edge of these multicellular aggregates correlate with alignment in this direction of the principal stress vector in cells behind them, a phenomenon called plithotaxis, which has been implicated in collective cell migration (Zaritsky et al., 2015). Finally, stress inference from TFM has also shown that stresses at the cell–cell junctions are higher in the island center and become smaller in the periphery, where traction forces are higher (Trepaut et al., 2009; Mertz et al., 2013; Ng et al., 2014). Results from these experiments further revealed mechanical cross-talk between both cell–cell and cell–substrate adhesion systems (Martinez-Rico et al., 2010; Jasaitis et al., 2012; Weber et al., 2012; Mertz et al., 2013).

Recently the Prost lab developed a theoretical framework, incorporating adhesion between cells and their substrate, for the analysis of the physical behavior of epithelial sheets and how it defines different properties of the tissue in three dimensions (Hannezo et al., 2014). In addition, particle-based simulation approaches have been used to model the dynamics of adhesive clusters that have been successful in predicting the pattern of forces developed by cell aggregates (Zimmermann et al., 2014, 2016). However, these models lack important physiological features of cells, such as cell protrusions, cell–substrate adhesion, and/or cell–cell junctions, limiting their ability to incorporate experimental data about these features. Finally, vertex and cellular Potts models have been extensively used to describe the physical state of epithelial cells. In particular, in vertex models, cells are modeled as polygons, and the position of the vertex is varied according to a probabilistic rule that depends on the cell elasticity, junctional contractility, and cell–cell adhesion parameters (Farhadifar et al., 2007; Fletcher et al., 2014; Bi et al., 2015; Misra et al., 2016). On the other hand, in cellular Potts models, a cell is made up of a given number of pixels that are connected and allowed to change the index (cell) that has been assigned to them, so they go from belonging to one cell to belonging to another according to some probabilistic rule that frequently is very similar to the rules used to change vertex positions in vertex models (Kabla, 2012; Noppe et al., 2015; Magno et al., 2015; Albert and Schwarz, 2016). Together, vertex and cellular Potts models have been effective in

describing how cell packing and total interfacial tension depend on basic features such as cell contractility and cell–cell adhesion (Farhadifar et al., 2007; Noppe et al., 2015). However, by themselves, these models of cell–cell junctions are not well suited for discrete systems with few cells, for which adhesion to the substrate becomes more important as the size of the island becomes smaller.

Here we created a vertex version of our recently reported continuous model of confluent epithelial cells (Noppe et al., 2015) in which cells are also able to interact with the substrate and exhibit contact inhibition of locomotion (CIL; Coburn et al., 2013). Using this model, we analyzed the traction force, monolayer stress, and junctional tension distribution of discrete epithelial systems (~10–300 cells) and made comparisons with experimental data. We found that the model reproduced well previous experimental observations on the distribution of traction forces and monolayer stress at cell–cell junctions and also showed the presence of plithotaxis and mechanical cross-talk between both adhesion systems. It also predicted that junctional tension is not homogeneous along the island but instead scales up with island size, which we confirmed experimentally by using laser ablation. Thus our model can generate emergent properties of epithelial cells, which can aid in the analysis of epithelial tissue mechanics.

RESULTS

Model of epithelial cells

To build our model, we considered that the biomechanics of epithelial cells can be analyzed in terms of the behavior of 1) their basal surface, which interacts with the substrate and forms protrusions; and 2) the cell–cell interface, where cells adhere to one another and which exhibits contractile properties (Wu et al., 2014). The model then takes into account that these two features are coupled mechanically through the body of the cell, which has some degree of intracellular stiffness (Figure 1A). This constitutes a first simplification to focus on two important features of epithelial cells. Although, strictly speaking, the model does not aim to describe the

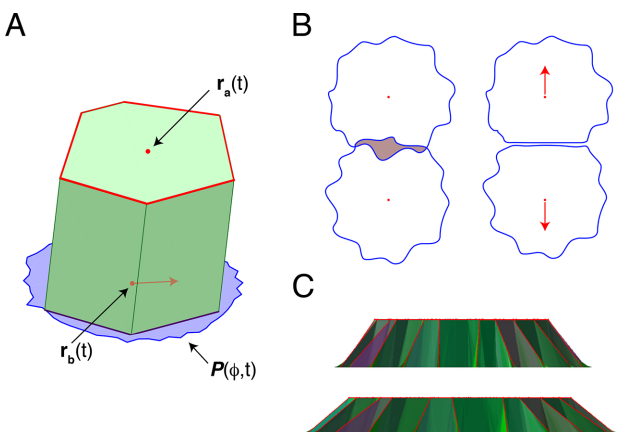


FIGURE 1: Model of epithelial cells. (A) Cells are represented as skewed prisms sitting on top of a zero-volume contour, $P(\phi, t)$, representing the cell–substrate interface (basal protrusions). The horizontal distance between the apical ($r_a(t)$) and basal ($r_b(t)$) centroids is measured. (B) CIL interaction results in a retraction of the overlapping segments in the radial direction for each cell, thus breaking the symmetry of the protrusion contour for each cell. As a result, both cells gain net traction in the direction of the asymmetry. (C) Epithelial cells are free to expand and contract. However, varying the height of the apical surface conserves the total volume of the monolayer.

three-dimensional (3D) properties of cells, with the foregoing simplifications, we propose a computational approach for the analysis of the biomechanics of epithelial cell aggregates based on the coupling of our previously reported algorithms for cell-cell adhesion and cell-substrate adhesion.

Cell-cell adhesion and junctional contractility

A common way to model the apical cell-cell junctions and the apical surface of epithelial tissues is by the use of vertex models (Farhadifar et al., 2007; Canela-Xandri et al., 2011; Bi et al., 2015). In this approximation, the tissue or cell aggregate surface is represented by connected polygons in the two-dimensional (2D) plane where cell-cell interactions occur. Within this plane, each polygon corresponds to one cell, the edges between two polygons correspond to a cell-cell junction, and vertices correspond to points where three or more cells meet. The energy (E_i) for the i th cell is then calculated from

$$E_i = -J \sum_{j=1}^n l_j + K \sum_{j=1}^n l_j^2 + \lambda [a_i - a_o]^2 \quad (1)$$

where a_i is its apical surface area, l_j is the cell contact length between two cells, n is the number of contacts that the i th cell make with its neighbors, and a_o is the preferred apical surface area for all cells. The parameters J , K , and λ are the system parameters that weight the contribution of adhesion, junctional contractility, and volume elasticity (at constant cell height), respectively. The first term in Eq. 1 is the cell-cell adhesion term and becomes more negative as the perimeter elongates, reflecting the capacity of cells to adhere to one another. The second term in Eq. 1 is related to junctional contractility, which tends to reduce the contact length (and the cell's perimeter) and thus generates junctional tension. The third term in Eq. 1 relates to the cell's elasticity, with cells allowed to have a variable shape but with their volume kept constant (see later discussion) by varying their apical area around a target area a_o . The last term finds a minimum when $a_i = a_o$, that is, when cells acquire their preferred apical area.

The total energy of the system (E_T) for a given configuration of vertices is given by $E_T = \sum_{i=1}^N E_i$, where N is the number of cells present in the aggregate. A typical simulation starts with cells configured into a square lattice, and then, by following a Monte Carlo algorithm, we update the vertex positions until we obtain a stable configuration. More specifically, in a single Monte Carlo step (MCS), a vertex is randomly selected, and one of the following processes is performed: the vertex 1) is moved by a distance dr in a random direction, where $dr = 0.1$; 2) split into two vertices by defining a new vertex and hence generating a new bond connected to the chosen vertex (junction formation); or 3) destroyed by selecting a bond and removing one of the vertices at its end points (junction removal). In each MCS, these three processes have equal probability of being selected at the same time that internal angles defined by two consecutive junctions in a cell are limited to the range $[0, \pi]$. After this change is made, the variation in the total energy of the system, $\Delta E_T = E_T(\text{after}) - E_T(\text{before})$, is calculated based on Eq. 1, and the update is made according to a Metropolis procedure: if $\Delta E_T < 0$, then the change has led to a reduction in energy and will be accepted. If $\Delta E_T > 0$, the change can still be accepted with a probability $e^{-\Delta E_T/\chi}$, where χ is the noise parameter. To map the dynamics of the junctions at the apical surface onto the dynamics of the basal surface (see later discussion), we assume that one time step corresponds to a Monte Carlo cycle (number of vertex MCS attempts on random selected vertices). Simulations were performed with values of $a_o = 1$ and $\lambda = 0.5$ unless otherwise specified.

Cell-substrate adhesion and cell motility

To introduce adhesion to the substrate and cell motility, we modified our previous CIL algorithm (Coburn et al., 2013). Briefly, in this model, cells are allowed to adhere to their substrate, spread their basal area, and extend protrusions in the direction that they migrate, similarly to real cells when they migrate into a free surface. If an asymmetry in the protrusions is present (i.e., a net force of traction on the cell exists), then the cell will move in the direction of the asymmetry (Caballero et al., 2014; Wong et al., 2014). We use this behavior to incorporate motility into our simulation (Coburn et al., 2013). Then the contact-inhibition-of-locomotion process (Roycroft and Mayor, 2016) is incorporated into the Monte Carlo scheme as follows: if, after a Monte Carlo cycle, the basal layer of two cells overlaps, cell protrusions are then retracted from the area of overlap in the radial direction toward their own cell center. This results in an alteration of the distribution of cell protrusions and a net change in the force of traction and cell orientation (Figure 1B).

In the simulations, time-averaged cellular protrusions are distributed uniformly around a cell. We represent this as a closed curve about a center point, $r_i^b(t)$, that is updated after a Monte Carlo cycle. The initial basal perimeter P is represented in polar form as (see also Figure 1A)

$$P_i(\phi) = 0, \quad 0 < \phi < 2\pi \quad (2)$$

Cellular protrusions then relax to a time-averaged uniform distribution, $P_0(\phi) = A_1$, over the subsequent time steps. Here ϕ is represented as a discrete set of m values with $\phi_j = 2\pi j/m$, $j = 1, \dots, m$ and $m = 50$. To have an estimation of A_1 , we performed different simulations of cell islands, varying this parameter, and measured the average basal-to-apical area ratios of cells. We then compared these values to those derived from experiments with the same number of cells in the island. We found that a value of $A_1 = 0.8$ generates an apical-to-basal area ratio in the simulations that fits with those observed experimentally.

In the numerical simulations, protrusion contours are updated using discrete time steps in which cells gradually remodel their protrusions around the target perimeter $P_0(\phi)$ according to

$$\frac{dP_i(\phi, t)}{dt} = -\gamma [P_i(\phi, t) - P_0(\phi)] + \xi(\phi, t) \quad (3)$$

where γ determines the rate of regrowth. Random fluctuations are incorporated into the protrusion contour by adding an uncorrelated white noise function $\xi(\phi, t)$ with noise intensity p , where

$$\langle \xi(\phi, t) \xi(\phi, t + \tau) \rangle = p^2 \delta(\tau) \quad (4)$$

Finally, to relate cell traction forces to their motility, we assume that cellular protrusions impart a net force on the cell in the direction of migration that is proportional to the degree of asymmetry of the distribution of protrusions around the cell. For real cells, this assumption is valid within times scales on which asymmetry in protrusions, cell velocity, and the presence and direction of traction forces are correlated (Caballero et al., 2014) but not on shorter time scales, on which there is a time delay between the occurrences of these phenomena (Notbohm et al., 2016). This is related to the underlying mechanotransduction processes that occur at focal adhesions before cells exert forces on a new area of cell-substrate attachment (Wong et al., 2014). With this assumption, we then define the total force that protrusions apply on the i th cell, $F_p^i(t)$, to be the integral of the protrusion lengths in all directions about the center of the cell:

$$\mathbf{F}_p^i(t) = h_o \int_0^{2\pi} P_i(\phi, t) u_\phi d\phi \quad (5)$$

where h_o is a prefactor related to the capacity of cells to adhere to their substrate and cell motility (which also depend either on the presence of ligands and/or substrate mechanical properties), u_ϕ is the radial unit vector in the direction ϕ , and $P_i(\phi, t)$ is the protrusion contour of the i th cell at time t .

Coupling between cell-cell adhesion and cell-substrate adhesion and contribution of intracellular cell stiffness to cell motility and apical cell interactions

Finally, to couple the apical and basal layers of the in silico cells, we approximate them as skewed prisms with parallel apical and basal surfaces with centroids $\mathbf{r}_i^a(t)$ and $\mathbf{r}_i^b(t)$, respectively (Figure 1A). These surfaces sit on top of a 2D protrusion contour ($P_i(\phi, t)$) that determines the position of the basal centroid. Then, for a randomly moving cell, attachment to a neighbor limits its freedom, and this can be represented as a damping of its motility. This damping also depends on the stiffness of the cell and how deformable it is, which ultimately depends on the properties of the cortical actin cytoskeleton. For this reason, we include an extra term in the cell motility description to account for this effect. Although the cell cytoskeleton is an overdamped network of different biopolymers, we assume that over short time scales, it has an intrinsic stiffness and behaves as an elastic spring with constant s , which determines how the force is transmitted through the cell interior. This is included in the foregoing CIL model by introducing an additional spring term for the horizontal displacement between the $\mathbf{r}_i^a(t)$ and $\mathbf{r}_i^b(t)$ centroids,

$$\frac{d\mathbf{r}_i^b(t)}{dt} = \mathbf{F}_p^i(t) - s\Delta\mathbf{r}(t) \quad (6)$$

where $\Delta\mathbf{r}(t) = \mathbf{r}_i^a(t) - \mathbf{r}_i^b(t)$. Thus the second term in Eq. 6 acts against the force due to cell protrusions and limits the offset between the apical and basal surface of a cell. Using Eq. 6, we update the position of the basal surface following the first-order Euler scheme

$$\mathbf{r}_i^b(t + dt) = \mathbf{r}_i^b(t) + \frac{d\mathbf{r}_i^b(t)}{dt} \Delta t$$

where Δt corresponds to a Monte Carlo cycle (or one simulation time step).

Similarly, the intracellular cell stiffness is also incorporated into the apical layer (Eq. 1) by including a spring term ($cs|\Delta\mathbf{r}(t)|^2$) in the energy function:

$$E_i = -J \sum_{j=1}^n l_j + K \sum_{j=1}^n l_j^2 + \lambda [a_i - a_o]^2 + cs|\Delta\mathbf{r}(t)|^2 \quad (7)$$

where c is a scaling factor. This term has a minimum when the horizontal displacement between the apical and protrusion centers is zero ($|\Delta\mathbf{r}(t)| = 0$), which is the case for confluent epithelial cells layers analyzed under periodic boundary conditions.

Cell volume preservation

We performed two types of simulations, depending on the boundary conditions: 1) periodic boundary conditions to model confluent monolayers, and 2) nonperiodic/semiperiodic boundary condition to model cell islands and stripes in which some boundary layer cells will "see" free space instead of another cell. In our simulations using periodic boundary conditions, we assume that the cell volume is conserved locally by changes in monolayer height, as in Farhadifar et al. (2007). In contrast, for simulations with open boundaries

(islands), the apical surface area is free to expand or contract. To conserve cell volume, the height of the monolayer, which we assume to be constant for bulk cells, is varied. To better illustrate this point, Figure 1C shows an example of two islands with the same volume but different apical surface area and height.

Approach to modeling cell stripes and islands

As mentioned earlier, we will consider the scenario in which some cells are not completely surrounded by other cells. At the border between a cluster of cells and the free space, one can expect a growth of cellular protrusions toward the free space (Poujade et al., 2007; Trepat et al., 2009). Thus parameters defining the protrusion sizes, traction forces, and intrinsic cell stiffness can be adjusted using experimental data derived from small islands (<10 cells). We varied the ratio of basal cell area to apical cell area and the absolute value of the average horizontal offset between apical and basal centroids to match parameters for protrusions between simulations and experiments. In addition, because islands of cells are no longer periodic (and their area is not fixed), the total apical area of stripes and islands can decrease or expand beyond the preferred apical area observed in confluent monolayers. For a better comparison between behavior of the cells at the different positions of the island or stripe, averages of traction and tension are shown only for bulk cells (i.e., row cell number >1).

Mechanics of confluent epithelial cell monolayers

Hard and soft regimes within confluent epithelial cell monolayers. Junctional tension makes epithelial tissues more rigid. In the model, the presence of junctional tension is determined by the presence of positive interfacial tension (Magno et al., 2015), according to the equation

$$\frac{dE_i}{dl_i} > 0 \quad (8)$$

Hard and soft regimes thus can be defined by the presence of positive or negative interfacial tension, (dE_i/dl_i) , respectively. Although adhesion to the substrate is present in the model, for simplicity, we can neglect its contribution in the analysis of confluent monolayers because under these conditions, protrusions symmetrically distribute around the cell-substrate interface, and within a monolayer, apical and basal centroids are effectively aligned; therefore $cs|\Delta\mathbf{r}(t)|^2 = 0$. Supporting this assumption is the fact that the boundary between soft and hard regimes in confluent monolayers is not affected by varying the motility and cell stiffness parameters (Figure 2D). Using this result and taking the derivative of Eq. 7, we then obtain

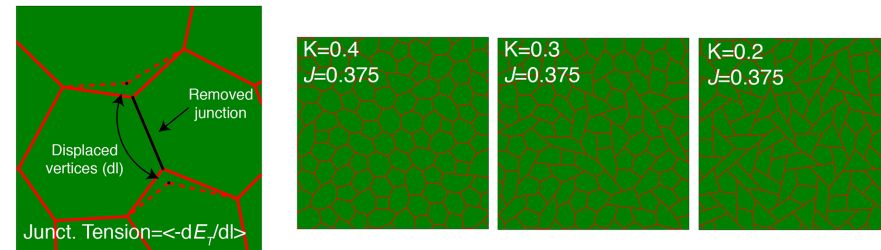
$$\frac{dE_i}{dl_i} = -J + 2Kl_i + 2\lambda [a_i - a_o] \frac{da_i}{dl_i} \quad (9)$$

We then consider the case of epithelial monolayers formed by cells with regular polygonal shape (i.e., all n sides equivalent, $l_1 = l_2 = l_3 = \dots = l_n = l_i$), which can uniformly pack or tile a surface without leaving gaps. Although regular pentagons ($n = 5$) cannot tile a surface uniformly, the following equations constitute an approximation for cells with irregular pentagonal shape. Thus, for regular polygons, it is possible to write the following relationships between polygon area, a_i , perimeter, p_i , and side (or cell-cell contact) length, l_i (Supplemental Figure S1; Staple et al., 2010; Magno et al., 2015):

$$\sum_{j=1}^n l_j = nl_i = p_i \quad (10)$$

A

B



C

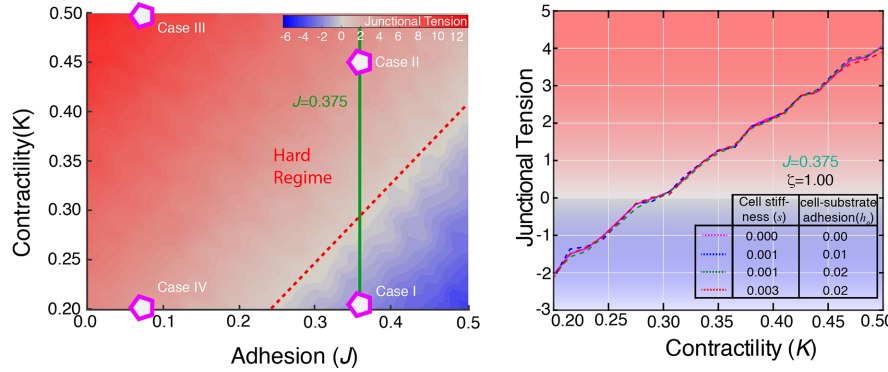


FIGURE 2: Mechanics of confluent monolayers. (A) Schematic of the tension calculation. Once simulations reach the steady state, a cell–cell junction is selected and removed, and the total energy of the system is calculated. The junction is then extended by a distance dl , and the resulting change in energy is measured. Tension is then calculated as $T = -(dE_J/dl)$. (B) Freeze-frame of borderless monolayers for three values of contractility, $K = 0.2, 0.3$, and 0.4 . (C) Phase diagram of tension, varying adhesion (J) and contractility (K). The highest junctional tension corresponds to higher values of the contractility and lower values of adhesion terms. The red dotted lines correspond to the theoretical boundary between hard and soft regimes according to Eq. 24. The green line corresponds to constant adhesion, $J = 0.375$. (D) Simulations varying the contractility (K values) at constant adhesion ($J = 0.375$, green line in C). Cell substrate adhesion (h_0) and stiffness (s) parameters were also varied as indicated in the inset table.

$$\sum_{j=1}^n l_j^2 = n l_i^2 = \frac{p_i^2}{n} \quad (11)$$

and

$$a_i = \frac{1}{4n} \cot\left(\frac{\pi}{n}\right) p_i^2 \quad (12)$$

Introducing the polygonal shape descriptor $\eta = \frac{n}{4} \cot\left(\frac{\pi}{n}\right)$, we can then write

$$a_i = \frac{n}{4} \cot\left(\frac{\pi}{n}\right) l_i^2 = \eta l_i^2 \quad (13)$$

Replacing these equalities into Eq. 9 gives

$$\frac{dE_i}{dl_i} = -J + 2Kl_i + 4\lambda a_0 \left(\frac{a_i}{a_0} - 1 \right) \eta l_i \quad (14)$$

For confluent epithelial monolayers, Eq. 14 can be further simplified by considering that cells cover the entire underlying surface and each cell acquires on average an area \bar{a} given by

$$\bar{a} = \frac{A_T}{N} \quad (15)$$

where A_T is the total area that the cells cover and N is the number of cells in the system. Note also that a_0 is the preferred area of cells, and it thus is possible to define a factor ζ that relates

to monolayer confluence (or cell packing density),

$$\zeta = \frac{\bar{a}}{a_0} \quad (16)$$

When $\zeta > 1$, cells cover the surface but do so by extending their area to greater than the preferred area (this scenario corresponds to the case in which the number of cells is suboptimal to cover the surface). In the other case, when $\zeta < 1$, cells are densely packed, and their average area is less than their preferred area.

Given this last consideration, it is then possible to rewrite Eq. 14 as

$$\frac{dE_i}{dl_i} = -J + 2Kl_i + 4\lambda a_0 (\zeta - 1) \eta l_i > 0 \quad (17)$$

which corresponds to the zeroth-order Taylor approximation at $l = \sqrt{a_0/\eta}$. From Eq. 17, the equilibrium cell–cell contact length, l^* , for a junction that is not under tension or compression is given by

$$\frac{dE_i}{dl_i} = -J + 2Kl^* + 4\lambda a_0 (\zeta - 1) \eta l^* = 0 \quad (18)$$

Whereas one of the solutions to Eq. 18 corresponds to the simple case in which cells are optimally packed, that is, $\bar{a} = a_0$ and $\zeta = 1$, and thus $l^* = l_0 = \frac{J}{2K}$, its more general solution is

$$l^* = \frac{l_0}{1 + \frac{2\lambda a_0 \eta (\zeta - 1)}{K}} \quad (19)$$

For physically meaningful solutions, we require $l^* > 0$. Thus

$$\zeta > 1 - \frac{K}{2\lambda a_0 \eta} > 0 \quad (20)$$

It is also possible to solve Eq. 17 to determine when cells within a monolayer with a given density and polygonal arrangement and junctions of length l_i will have a positive value of junctional/interfacial tension ($dE_i/dl_i > 0$). This is given by meeting the following condition:

$$l_i > l_i^* = \frac{l_0}{1 + \frac{2\lambda a_0 \eta (\zeta - 1)}{K}} \quad (21)$$

If we consider a confluent monolayer covered uniformly by polygons of the same shape, we can rewrite Eq. 21 as

$$l_i = \sqrt{\frac{\bar{a}}{\eta}} = \sqrt{\frac{a_0 \zeta}{\eta}} > \frac{l_0}{1 + \frac{2\lambda a_0 \eta (\zeta - 1)}{K}} \quad (22)$$

Replacing $l_0 = J/2K$ and rearranging to solve for K , we obtain then for the hard regime

$$K > \sqrt{\frac{\eta}{4a_0 \zeta}} J - 2\lambda a_0 \eta (\zeta - 1) \quad (23)$$

and the expression

$$K^0 = \sqrt{\frac{\eta}{4a_0\zeta}} J - 2\lambda a_0 \eta (\zeta - 1) \quad (24)$$

defines the line in the phase diagram that delimits the presence of cells with positive or negative interfacial/junctional tension.

Numerical simulations of confluent epithelial cell monolayers. To validate the model, we perform simulations of confluent monolayers to compare the model's behavior to the foregoing theoretical predictions (Figure 2). First, to characterize the amount of junctional/interfacial tension, we analyze the net force exerted on cell vertices when individual cell-cell junctions are removed (Figure 2A). Under this definition, negative values of force correspond to junctions under compression, whereas positive values denote junctions under tension. For each junction and configuration, we calculate an ensemble average of junctional tension by first removing a cell junction and then calculating the change in the energy of the system dE_T after dragging apart its vertices by an amount dl . Thus the tension on each junction is calculated as $T = -(dE_T / dl)$ (Figure 2A), for which the distance dl is reduced until the values obtained for the tension converge. This approach is comparable to the experimental situation in which a cell-cell junction is cut by laser ablation (Gomez et al., 2015).

Simulations were performed varying the parameters that control cell-cell adhesion energy (J) and junctional contractility (K). In agreement with previous simulations using vertex and cellular Potts models (Farhadifar et al., 2007; Noppe et al., 2015), we found that for high ratios of contractility to adhesion (K/J), cells acquire regular hexagonal order, whereas when the adhesion term is more prominent (low K/J values), the regular packing of cells is lost (Figure 2B). We then calculated the average junctional tension for the contacts in the lattice as a function of the adhesion (J) and contractility (K) parameters to create a phase diagram (Figure 2C) and compared it with our theoretical predictions (Eq. 24). We found that regions where the packing is more regular correspond to overall high junctional tension (hard regime), whereas irregular packing with less-ordered polygonal shapes is observed in systems having lower junctional tension (soft regime; Figure 2C). We also found that there is a boundary between regions with positive and negative junctional tension, in excellent agreement with our theoretical description and the predictions using Eq. 24 (red dotted line in the phase diagram).

To characterize further the system and define whether a phase transition occurs from the soft to the hard regime when contact contractility increases, we performed simulations with a constant cell-cell adhesion parameter ($J = 0.375$) while increasing contractility (K) systematically (Figure 2D). We observed a transition in the amount of junctional tension at contractility values $K \sim 0.3$, that compares well with the analytical prediction of Eq. 24 (Figure 2C). This suggests that, under these conditions, the effect of increasing contractility not only rigidifies the entire system but also collectively affects epithelial cell organization.

We then sought to elucidate the role of cell-substrate interactions and cell propulsion in the onset of hard and soft regimes in confluent monolayers. We performed the simulations presented in Figure 2D, varying the cell substrate interaction term h_0 , which defines the speed at which cells can move in the absence of cell-cell adhesion (Coburn et al., 2013). We found that introducing motility to cells does not alter the qualitative behavior of the model in simulations of confluent cell monolayers. A similar result was obtained when the cell stiffness parameter, s , was modified. Taken together, the results of the model suggested that within confluent monolayers, cell motility contributes neither to increasing the forces on

cell-cell junctions nor to the mechanics of cell-cell junctions. This response results from the fact that under these conditions, no net cell asymmetry in the basal layer is favored, and therefore the term $cs|\Delta r(t)|^2$ becomes negligible.

To evaluate further the performance of our modeling approach, we performed experiments (see Materials and Methods for more details) in which we analyzed the morphology of confluent cell monolayers treated with the myosin II inhibitor blebbistatin or dimethyl sulfoxide vehicle (control, Figure 3A). We then compared our empirical results to four *in silico* cases: I) $J = 0.375$, $K = 0.2$ (soft regime); II) $J = 0.375$, $K = 0.45$ (hard regime with high adhesion); III) $J = 0.075$, $K = 0.5$ (hard regime with low adhesion energy; see also Figure 2C); and IV) $J = 0.075$, $K = 0.2$ (hard regime with low adhesion and contractility). We recorded the cell shape distribution and polygon number of cells in simulations and experiments and compared the ratio of average area in a polygon class to average area, a_n/a , versus polygon number as previously described (Farhadifar et al., 2007; Canela-Xandri et al., 2011; Figure 3B). We found that in control cell monolayers, the rate of change of a_n/a with the polygon number is similar to that in cases in which cells exhibit high junctional tension (case II and, to a limited extent, case III; Figure 3B), in agreement with the fact that under normal circumstances, cell junctions are under tension (Wu et al., 2014; Gomez et al., 2015). Moreover, we found that when myosin II is inhibited, the rate of change of a_n/a with polygon number behaves similarly to that for control cells (case II), suggesting that in addition to inhibition in junctional contractility, cell-cell adhesion energy could be also compromised under these experimental conditions. This notion agrees with earlier evidence that myosin activity and junctional tension are required for the stability and accumulation of E-cadherin adhesion molecules on cell-cell junctions (Shewan et al., 2005; Rauzi et al., 2010; Smutny et al., 2010) and with numerical results in which we lowered adhesion as well as contractility (case IV, Figure 3B) and observed a similar rate of change of a_n/a with polygon number to the case of cells with higher adhesion and contractility (case II). Thus our modeling approach correlates well with the behavior observed in confluent monolayers of epithelial cells.

Mechanics of epithelial cell islands and stripes

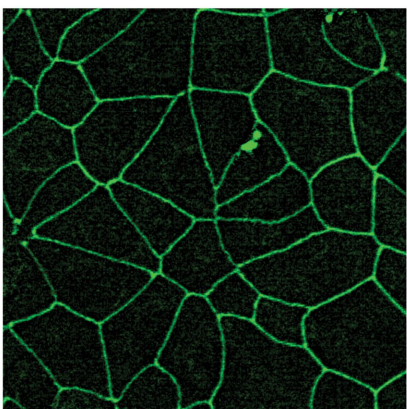
Force distribution in epithelial cell islands and stripes. To quantify the stress distribution in small epithelial cell aggregates, we modeled groups of cells forming stripes and islands (Figure 4A) and analyzed the steady-state distribution of monolayer stress and traction forces from the edge to up to 10 cell diameters (rows) inside the cluster. The total traction that epithelial cell islands or stripes apply on their substrate is calculated as a function of the distance from the edge, r , as the average projection of \mathbf{F}_p^i (Eq. 5) in the horizontal or radial directions for stripes and islands, respectively (see also Figure 4B):

$$\text{Tr}(r) = \mathbf{F}_{p,r} \quad (25)$$

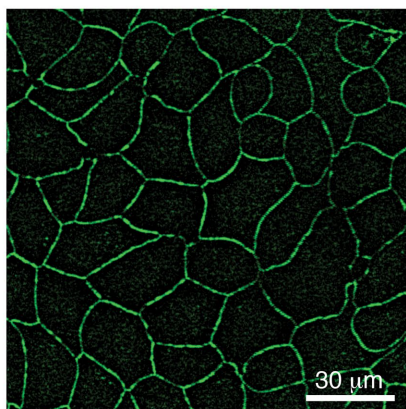
The presence of traction forces generates physical stress across the cell monolayer that is transmitted through the cytoskeleton and cell-cell junctions (Trepat et al., 2009; Liu et al., 2010; Maruthamuthu et al., 2011; Ng et al., 2014). At a specific position r from the edge, these traction forces are balanced by the local stresses in the cell monolayer (Trepat et al., 2009). Therefore, at a specific distance r from the edge, the sum of traction forces is balanced by the local stress in the monolayer at that position, allowing us to calculate this monolayer stress in the model as a function of the distance from the cell edge as

A

Control



Blebbistatin



When we analyzed the monolayer stress profiles, we found that for islands and stripes, the stress is higher at the center but lower in the periphery (Figure 4C). Overall the pattern observed for traction forces and monolayer stress for cell islands correlated well with previous results obtained experimentally with similar cell cultures (Trepat et al., 2009; Maruthamuthu et al., 2011; Ng et al., 2014).

On the basis of these results, we then investigated how those cells away from the island edge experience net traction forces. Cells at the edge have no neighbors outside the island, and their protrusions can extend more into the free space. Such asymmetry could be propagated, to some extent, inside the island, allowing cells in this location to generate traction forces. To analyze whether this is the case, we examined the degree of asymmetry between apical and basal cell areas ($|\Delta r_l|$) as a function of the distance from the edge, as a measure of the formation of cryptic lamellipodium in the model (Figure 4D). Similar to the traction force data, we found that the cells in the model exhibit a notable degree of asymmetry when located in proximity to the island and stripe edge. This degree of asymmetry is more pronounced in the direction orthogonal to the island edge than in the direction parallel to it (Supplemental Figure S2A) and decays with the cell position from the edge (Figure 4D and Supplemental Figure S2A), similar to what is observed in TFM of cell islands and during collective epithelial cell migration (Trepat et al., 2009; Das et al., 2015). We also considered the morphology of the apical region of cells and how the apical area orients with respect to the radial direction of the island. The results in Figure 4E show that cells preferentially elongate their apical area in the direction orthogonal to the island edge, meaning that its longer axis is oriented along the island's radial direction (average $\cos \theta \sim 0.4$ compared with average $\cos \theta = 0$ for a randomly oriented cell). Moreover, this degree of orientation penetrates several cell diameters within the island from its edge (Supplemental Movie S1). This resembles the phenomenon of plithotaxis during collective epithelial migration, in which the direction of the

B

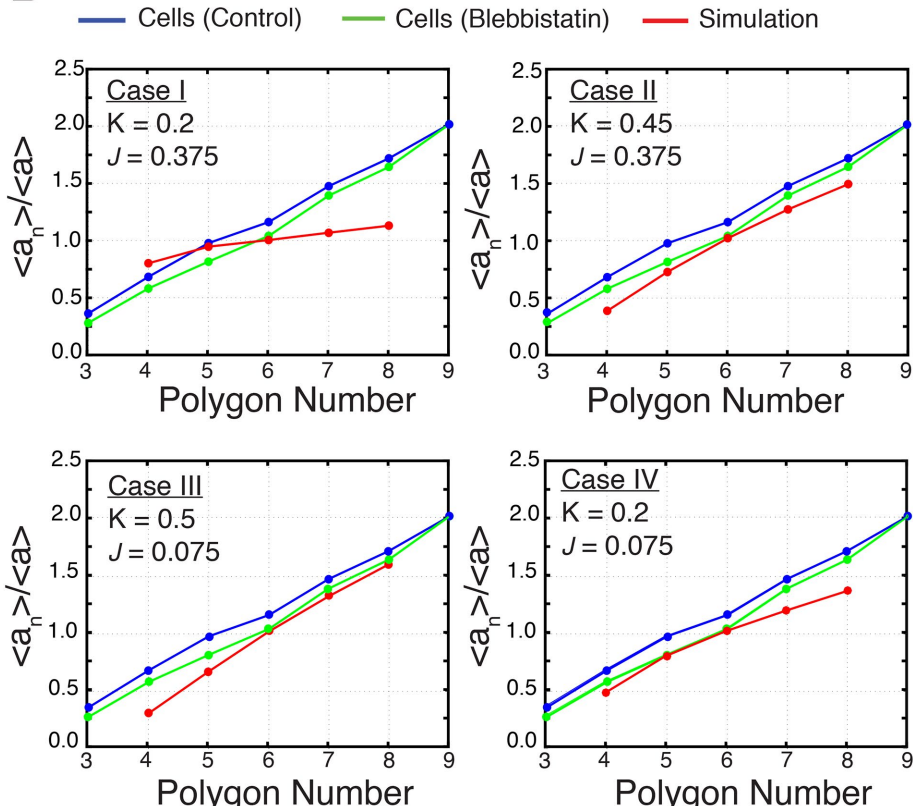


FIGURE 3: Analysis of cell morphology in confluent monolayers. (A) Images of control and blebbistatin-treated (100 μM , 2 h) confluent MCF-7 cell monolayers stained against the tight junction protein ZO-1. (B) Cell shape distribution in the experiments was measured as described in Materials and Methods and compared with that obtained in simulations (see also Figure 2C) by plotting the mean apical area in a polygon class over mean apical area ($\langle a_n \rangle / \langle a \rangle$) vs. polygon number. Case I, $J = 0.375$, $K = 0.2$; II, $J = 0.375$, $K = 0.45$; III, $J = 0.075$, $K = 0.5$, IV, $J = 0.075$ and $K = 0.2$.

$$\sigma(r) = \sum_{r=0}^r \text{Tr}(r) \quad (26)$$

We found that for both cell stripes and islands, traction forces are higher for cells at the edge and lower for cells at the center. Moreover, there are still significant (although smaller) traction forces for cells located in the third and fourth row behind the edge (Figure 4C; see also later discussion of Figure 6, Ai and Bi), suggesting that these cells still have the capacity to pull the island in the outward direction.

cell's principal stress is parallel to the direction of the cell's velocity (Zaritsky et al., 2015), which, in our case, is defined by the CIL process. Of note, we also found that in the model, the formation of asymmetries in cell protrusions and their extension inside the island or stripe are positively regulated by the motility of cells and negatively regulated by the cell stiffness (Supplemental Figure S2, B and C). Taken together, these results agree with experimental analysis of lamellipodium formation during epithelial cell migration (Abreu-Blanco et al., 2012; Anon et al., 2012; Das et al., 2015), the observed

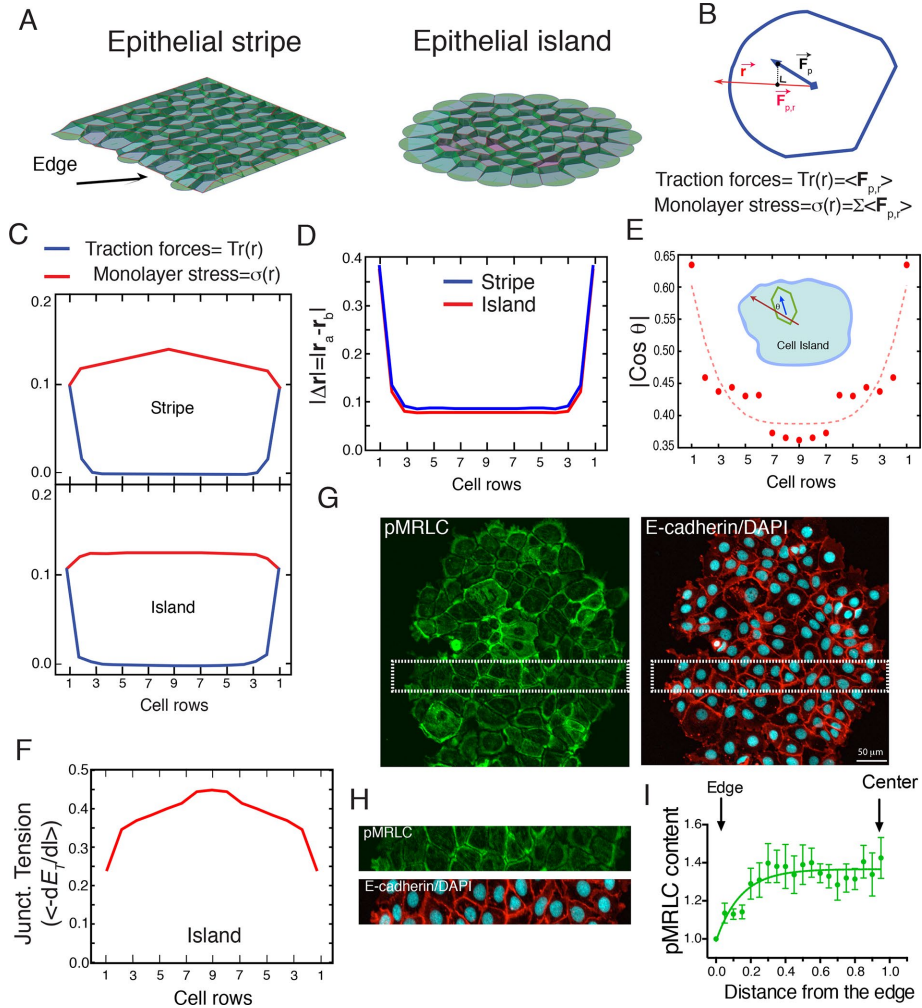


FIGURE 4: Mechanics of epithelial cell islands and stripes. (A) Cell stripes and islands in the simulation. (B) The magnitude of horizontal/radial traction, $|F_{p,r}|$, is calculated by projecting the cell traction vector, $\mathbf{F}_{p,r}$, onto the horizontal/radial direction, r . (C) Traction and monolayer stress in the radial direction across the island and stripe. (D) Plots of horizontal displacement (offset) between apical and basal centroids, $|\Delta r(t)|$, across islands and stripes. (E) Plot of $|\cos \theta|$ the angle between cell apical area long axis and the island radial direction across an epithelial cell island. (F) Plots of junctional tension across an island. (G) Immunofluorescence of MCF-7 epithelial cell islands stained against pSer19MRLC (green), E-cadherin (red), and nuclei (DAPI, cyan). (H) Magnification of regions indicated by the white rectangles in G. (I) Quantitation of pSer19MRLC (pMRLC) radial content as a function of the distance from the island edge.

cryptic lamellipodia underneath cells located toward the edge of the island (Farooqui and Fenteany, 2005; Trepat et al., 2009), and the alignment of the apical area of cells in the velocity direction as observed during plithotaxis (Zaritsky et al., 2015).

Because the model predicts a pattern of stresses similar to what is observed experimentally, we then investigated what property in the model accounts for the generation of this monolayer stress. We consider that the stress in the apical region of cells could be generated by the resistance of cells to deformation of their apical area or by an increase in the amount of tension at cell-cell junctions. To analyze the latter possibility, we performed numerical calculations of junctional tension as described in Figure 2A and plotted the results versus the distance of the particular junction from the island or stripe edge (Figure 4F). We found that under these conditions, junctional tension is lower in the peripheries of islands and stripes and higher in the centers, thus exhibiting a similar profile to the average stress in the monolayer and suggesting that cell junctions contribute significantly

to monolayer stress in the model. If this were the case in real cells, then our simulations predict that junctional contractility should exhibit the same pattern when analyzed in epithelial cell islands, that is, be lower in the periphery and higher in the center of the island. To test this, we analyzed the phosphomyosin regulatory light chain (pMRLC) content at cell-cell junctions in epithelial cell islands as a proxy for junctional contractility. In agreement with the model predictions, we found that pMRLC junctional content was lower at the island periphery and higher in the center (Figure 4, G–I).

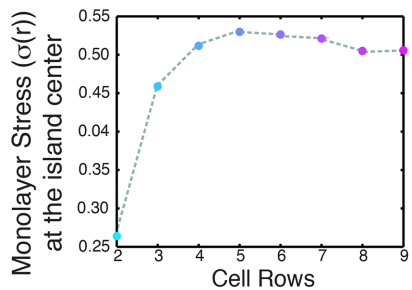
Effect of island size on epithelial mechanics.

Having found that the monolayer stress and junctional tension are higher at the island center, we used the model to explore whether this also depends on island size and compared this result with experimental data. We performed simulations of islands of different sizes and measured the stress and junctional tension at the center. We found that these parameters quickly scale up in islands of radius from two to six cell layers and then reach a plateau for bigger cell aggregates (Figure 5, A and B). We then performed laser ablation experiments on cell junctions located at the center of epithelial cell islands of different size to test the model's prediction. We grew epithelial cell islands to different sizes from single cells and measured initial recoil after laser ablation on a single junction per island as described previously (Gomez et al., 2015). In experiments using this assay, the measured amount of tension on junctions at the center of the islands increased with the size of the island, a result that agreed with the predictions of our model (Figure 5c). Thus our in silico and experimental results suggest that in cells, the amount of junctional tension is a collective emergent property of the system.

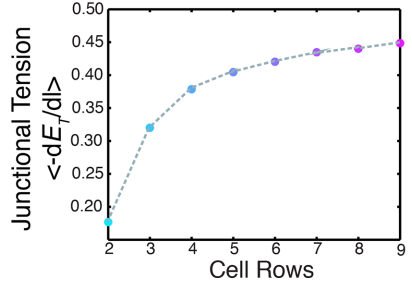
Mechanical cross-talk between cell-substrate and cell-cell adhesion sites. We then investigated whether junctional contractility and cell motility influence the patterns of traction force and junctional tension exhibited by epithelial cell islands by testing whether the model exhibits mechanical cross-talk between the cell–cell and cell–substrate adhesion systems.

We first performed a set of simulations varying the cell motility parameter and analyzed the distributions of traction force, monolayer stress, offset of apical and basal areas, and junctional tension (Figure 6A). As expected, we found that increasing cell motility leads to an increase in the amount of traction force and increases the offset between the apical and basal areas in the cells at the periphery of the island (Figure 6A, i and ii). More surprisingly, we found that the model exhibits some degree of mechanical cross-talk, as the amount of junctional tension also increased when cell motility increased (Figure 6Aiii). This suggested that in discrete systems of epithelial cell islands, cell motility

A



B



C

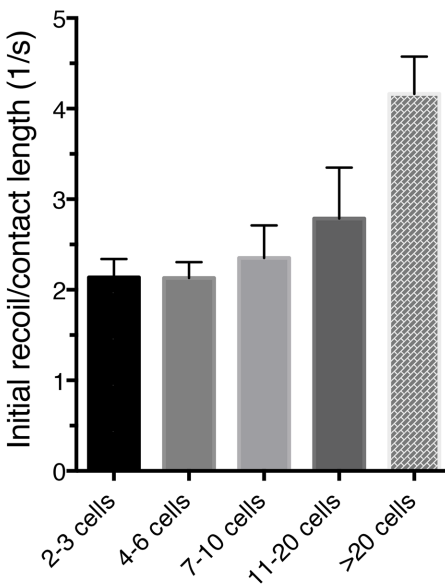


FIGURE 5: Effect of island size on its biomechanics. Basal stress (A) and junctional tension (B) at island center vs. island size (in rows) calculated from simulations. (C) Initial recoil/junction length measured at the center of MCF-7 cell islands of different sizes.

contributes to the amount of force that operates at cell–cell junctions.

We then also asked whether increasing junctional contractility in the model led to changes in traction forces and monolayer stress. We found that increasing junctional contractility leads to an increase in the amount of traction forces in the island periphery, as well as to an overall increase in the monolayer stress and junctional tension (Figure 6B, i and iii). This occurs together with an increase in the offset between apical and basal areas (cryptic lamellipodia index; Figure 6Bi).

These results show that a simple model that minimally integrates cell–cell adhesion and cell motility together with CIL produces a strong cross-talk between the adhesion systems and show how this interaction leads to different emergent properties of epithelial cells that have been observed experimentally. Overall these observations correlate well with the fact that the cell–extracellular matrix traction force modulates junctional tension (Liu et al., 2010; Maruthamuthu et al., 2011) and pulling forces on cadherin junctions lead to an increase in cellular traction forces (Weber et al., 2012; Mertz et al., 2013).

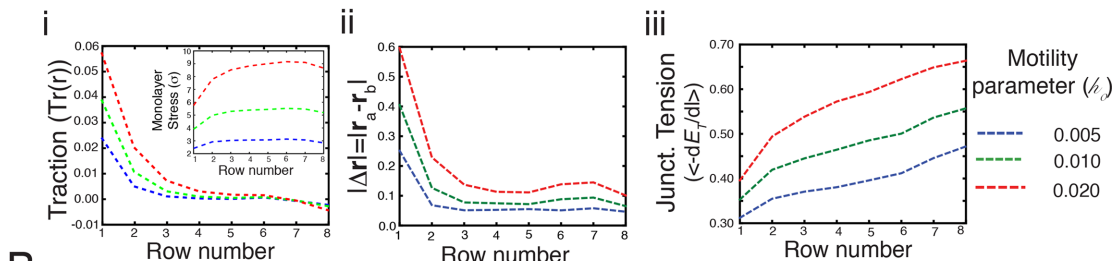
DISCUSSION

We developed a quasi-3D model of epithelial cells that includes their capacity to adhere to each other and to the substrate and exhibit contact inhibition of locomotion. In addition, cells in the model present intracellular stiffness and constant volume. Without being formally a 3D model, our approach has the analytical advantage of allowing direct extraction and comparison of cellular properties that can be measured experimentally. Parameters of the model such as

tension, cell motility, cell packing, and topology can also be introduced into it from experimental data. In particular, this aligns very well with many cases in which analysis of mechanical properties of epithelial cells are made assuming that such cells form a flat monolayer and this structure does not escape to the third dimension (e.g., form bends). Thus, although limited, this is a normal assumption that is made in experiments, and our model naturally captures it.

Our approach allows straightforward comparison between simulations and experimental data because many of the biophysical

A



B

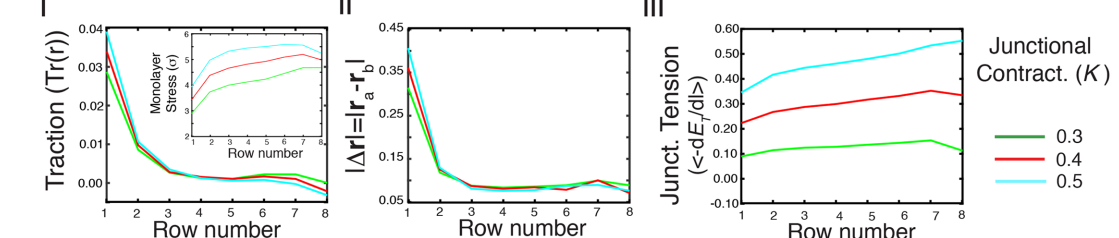


FIGURE 6: Mechanical cross-talk of adhesion systems in the model. Plots of (i) traction, basal stress, (ii) apical/basal offset, and (iii) junctional tension vs. row number for varying (A) cell–substrate adhesion (h_0) and (B) contractility (K). For these simulations, $J = 0.375$, $s = 0.001$, and $c = 0.4 \times 10^2$.

methods that are suited to assess the biomechanical state of epithelial cells in monolayers are based on approaches that test how cells interact with their substrate and/or approaches focused on the apical layer of cells (Polacheck and Chen, 2016). Examples of these methods include the use of TFM with monolayer stress inference calculations (Nier et al., 2016) and junctional tension, which can be measured by laser ablation (Caldwell et al., 2014) or optical tweezers (Bambardekar et al., 2015). The model also allows comparison of the topology of cell arrangements within the monolayer between simulation and experiment, which allows mechanical inference of the state of cells even without directly measuring tension and/or stress, thus complementing other methods of stress inference (Chiou et al., 2012; Sugimura and Ishihara, 2013). Accordingly, not only can the model be used to test predictions, but it can also be fed with experimental results obtained from these experiments. This contrasts with models that take into account only cell-cell interactions, for example (Farhadifar et al., 2007; Kabla, 2012), which work relatively well for local analysis of cells in relatively large tissues with negligible cryptic lamellipodia, thus matching the conditions of the confluent-monolayer cases analyzed in this work. Our model also contrasts with recent models that represent cells as particles (Zimmermann et al., 2016), which are computationally robust and can make good predictions but lack the capacity to use experimental snapshots of cell topology to infer the mechanical properties of the tissue. Finally, although our modeling approach does not necessarily represent cells in three dimensions, it is a practical and straightforward application for most of the available experimental data, which are not necessarily three dimensional. Of note, modeling in three dimensions requires extra measurements of parameters, which are not always possible to obtain directly or might be very difficult to measure, as are the variations in adhesion or tension in the xz-plane of the cell-cell interface (Wu et al., 2014).

Using our approach, we then developed a theoretical analysis complemented by numerical simulations on the presence of soft and hard regimes in confluent monolayers that correspond to cells exhibiting positive or negative values of interfacial/junctional tension (Farhadifar et al., 2007; Magno et al., 2015; Noppe et al., 2015). Results from the simulations showed perfect agreements with our theoretical predictions. Note that the soft/hard transitions described here are different from the jamming type of transition described recently by the Manning group (Bi et al., 2015) and observed experimentally (Park et al., 2015), in which the energetics associated with T1 transitions is described as a change in polygonal arrangement from hexagonal to pentagonal within the vertex model. Thus analyzing how adhesion to the substrate and CIL in expanding cell islands or during collective migration affect this type of transition constitute new areas that deserve further research.

When we applied our model to the mechanics of epithelial cell stripes and islands, we found that for discrete systems, the presence of a free boundary can polarize cell protrusions at the edge of an island, and this effect is propagated into the tissue to distances of several cell diameters. Because of this, islands and stripes develop patterns of traction forces, monolayer stress, and junctional tension that vary from the edge to the center of the multicellular aggregate. We further found that these patterns agreed very well with the experimental observations and with a recent report using a particle-based simulation model (Zimmermann et al., 2016). Of interest, our model allowed us to test the prediction that junctional tension at the center of islands increases with island size, which we confirmed experimentally using laser ablation. This can be explained in terms of the mechanics of epithelial cell islands because the amount of radial outward traction generated in an island is proportional to the num-

ber of cells at the edge, that is, to the island perimeter, which scales linearly with the island radius and as the square root of the area or the number of cells (at least for small islands). Because at the same time, the amount of stress decreases away from the edge of the island due to internal damping, this explains why it would not grow any further when the size of the island becomes very large. This is in agreement with what was previously shown about the dependence of traction forces on the size of the epithelial cell aggregate (Mertz et al., 2012). Thus our modeling approach is able to unify previous continuous approaches with a more discrete model into which individual cell properties are explicitly incorporated.

Our modeling approach also has the minimal properties that allow mechanical cross-talk between cell-cell and cell-substrate adhesion systems. Our simulations showed how the presence of developing traction forces is sufficient to increase junctional tension on cells behind the edge of the island. In addition, they showed how the presence of junctional contractility can also modulate the amount of traction force that cells exert on their substrate, which has been also observed experimentally (Jasaitis et al., 2012; Weber et al., 2012; Mertz et al., 2013).

Our results on islands and stripes agree with previous analytical descriptions of traction forces exerted by contractile cell layers (Edwards and Schwarz, 2011; Banerjee and Marchetti, 2012). Those studies found that higher traction forces are developed at the rim of the islands/stripes, and this results naturally from the solution of a finite-sized contractile layer coupled to an elastic substrate. In our model, these two properties are exhibited by the CIL component, which allows the island/stripe to exert forces that tend to increase the size of the island (similar to pillars in the description by Edwards and Schwarz, 2011), whereas contractile cells tend to shrink the island or stripe via volume conservation and contractile junctions.

Our modeling framework also recapitulates some of the pliotaxis properties exhibited by epithelial cells (Zaritsky et al., 2015). It has been shown that there is a correlation between the directions of migration and cellular principal stress, which has been confirmed experimentally. In our model, CIL on cells on the edge of the island allow those cells to polarize and maximize their velocity vector in the outward direction. Snapshots of the simulation showed that this leads to an increased aspect ratio of the cell in the radial direction, which is propagated several cell diameters inside the island (Figure 4E). This aspect ratio in the apical area of cells corresponds to the principal stress direction (the basal layer does not contribute to it because it does not have cell-cell interactions). We observe a similar effect in simulations of expanding cell islands, that is, when simulations were initialized with cells having an average cell area smaller than the preferred area, we observed finger formation on some leader cells and the alignment of major stress toward this direction for cells located several cell diameters behind them (Supplemental Movie S1). Our model does not make a distinction between cell motility and traction, however, and both vectors are aligned. Although this could be negligible on long time scales, recent analysis shows that on very short time scales, this might not be well correlated (Notbohm et al., 2016).

Our model also allowed us to investigate the propagation of forces within cell aggregates. In particular, we analyzed the effect of introducing four hypercontractile cells at the center of the epithelial cell island and analyzed how far force can be propagated. In agreement with previous experimental results (Ng et al., 2014), we did not observe a significant degree of force propagation within the island, which was limited to one to two cell diameters (Supplemental Figure S2D). This again highlights the mechanics of epithelial islands as an emergent property of the system by which the presence of adhesion

to the substrate limits the capacity of the tissue to exhibit force propagation within the system, as is discussed in more detail in Ng et al. (2014).

Although our modeling approach can be adapted very well for the analysis of epithelial cell organization in relatively flat tissues (2D-like systems), it is not suitable for the analysis of monolayer morphology in three dimensions. In particular, vertex models have been extended to three dimensions to analyze the epithelial cell-cell rearrangements that occur during cell extrusion and cyst formation (Bielmeier et al., 2016) and during ventral furrow invagination (Polyakov et al., 2014). Introducing CIL into these models would allow a more comprehensive view of the interplay between adhesion systems during these processes, which involve force propagation, cell rearrangement, and collective migration, and theoretical analysis has already started to highlight the role of mechanics during these 3D morphological changes in tissues (Hannezo et al., 2014).

Finally, so far, our model of epithelial cells recapitulates only passive mechanical properties of cells and points out a key role of CIL as a spatial clue that leads to the polarization of cell mechanics within epithelial cell aggregates. Such polarization seems to be a general characteristic of cells and has also been introduced to reproduce experimental observations in the context of wound healing and collective migration (Banerjee et al., 2015; Notbohm et al., 2016). Although described as a passive element in our model, it has become increasingly clear that CIL is an active process, and it was recently found that the switching of cadherin cell–cell receptors plays a key role in CIL (Scarpa et al., 2015). In particular, Scarpa et al. (2015) show that the presence of E-cadherin contact suppresses CIL, and its loss (or switch to N-cadherin) activates Rac1 signaling, thus allowing cells to exhibit CIL. In the context of cell islands, this could correlate with different levels of Rac activity at the cell–substrate interface, which is higher in cells in the periphery of the island and lower in cells located in the center. This could lead to a pattern of protrusive activity and CIL that is consistent with our numerical simulations. Moreover, our data show that pMRLC content is higher in the island center and lower in the island periphery, but how cells control this at the molecular level is less clear and perhaps reflects the capacity of E-cadherin–based junctions to support mechanotransduction (Gomez et al., 2011). Therefore it becomes important to characterize the mechanotransduction mechanisms that cells use to regulate both the amount of force that acts on these adhesion systems and CIL, which result in the pattern of traction forces and junctional tension observed both theoretically and experimentally. This will help us to understand how cells resist the increasing stresses that occur in response to local changes in cell mechanics and drive collective cell behavior and morphological transitions that occur, for example, during cell extrusion, wound healing, and cell migration and thus preserve tissue integrity.

MATERIALS AND METHODS

Immunofluorescence, microscopy, and analysis of cell morphology

Cells were fixed with 4% paraformaldehyde (PFA) in cytoskeletal stabilization buffer (Leerberg et al., 2014). Immunostaining was performed using rabbit anti-phospho-(Ser-19)-MRLC antibody (Ab; 36755; Cell Signaling, Danvers, MA), rat anti-E-cadherin Ab (ECCD-2, 13-1900; Invitrogen, Camarillo, CA), mouse anti-ZO-1 (33-9100; Invitrogen), and Alexa-conjugated secondary Abs (Molecular Probes, Eugene, OR) as appropriate. Coverslips were mounted in

Prolong Gold with 4',6-diamidino-2-phenylindole (DAPI; 8961; Cell Signaling). Confocal images were acquired on an LSM 710 laser scanning microscope (63x, 1.4 numerical aperture [NA] Plan Apo objective) driven by Zen software (ZEN 2009; Zeiss, Jena, Germany). Images of control and blebbistatin (203390; Merck, Darmstadt, Germany; 100 μM, 2 h)-treated cell monolayers stained against ZO1 were used to obtain histograms of cell morphology using the Packing Analyzer 2.0 software (Aigouy et al., 2010).

Quantitation of pMRLC fluorescence intensity in epithelial cell islands

For the quantitation of the radial distribution of pMRLC intensity in epithelial cell islands, we used the radial profile extended plug-in for ImageJ by Philippe Carl (Laboratoire de Biophotonique et Pharmacologie, Centre National de la Recherche Scientifique, Illkirch, France). Basically, a circle was drawn to enclose the edges of the island, and a sector with identical island radius (because, overall, islands are not fully symmetrical) was selected to measure the average intensity of pMRLC content. The obtained profiles were then normalized to the average intensity at the edge of the island, and the profiles were then averaged. Radial distances were rescaled to 0 (island edge) and 1 (island center) to normalize profiles across different islands. Data correspond to the average of 10 islands, and values are mean ± SEM.

Laser ablation experiments

Cells were grown to confluence on glass-bottom dishes, and cell medium was replaced with Hanks balanced salt solution (Sigma-Aldrich, St. Louis, MO) containing 5% fetal bovine serum, 10 mM 4-(2-hydroxyethyl)-1-piperazineethanesulfonic acid (15630130; Gibco, Carlsbad, CA), pH 7.4, and 5 mM CaCl₂ (Sigma-Aldrich) before imaging. The use of the laser ablation technique to assess junctional tension was described previously (Gomez et al., 2015). To assess junctional tension (Figure 5), cells stably expressing E-cadherin shRNA/E-cadherin–green fluorescent protein were used to identify the apical region of cell–cell contacts. All ablation experiments were carried out at 37°C on a Zeiss LSM510 system (40x, 1.3 NA Oil Plan Neofluar objective) using 17% transmission of the 790-nm laser on a 1 μm × 1 μm area on the apical junctions of cells. Time-lapse imaging of a 75 × 75-μm region was taken at 1.6-s intervals before (3 frames) and after (42 frames) ablation.

Data were analyzed in ImageJ, using the MTrackJ plug-in to track and measure the strain or deformation, $\epsilon(t)$, of the cell–cell junction as a function of time after ablation. Because on the time scales of our experiments junctional strain exhibit single-exponential growth with a defined plateau, this was then modeled as a Kelvin–Voigt fiber (Fernandez-Gonzalez et al., 2009; Michael et al., 2016) by fitting it to the following equation:

$$\epsilon(t) = L(t) - L(0) = \frac{F_0}{E} \left(1 - e^{-\left[\frac{(E)}{\mu} t \right]} \right)$$

where L is the length of the ablated junction, measured as the distances between the vertices that define it, F_0 is the tensile force present at the junction before ablation, E is the elasticity of the junction, and μ is the viscosity coefficient, related to the viscous drag of the medium. We used initial recoil = $d\epsilon(0)/dt = F_0/\mu$ and $k = E/\mu$ as fitting parameters for this equation. This model was used to calculate the initial recoil (the rate of recoil at $t = 0$) for each junction ablated.

ACKNOWLEDGMENTS

We thank all of our lab colleagues for support and advice. This work was supported by grants from the National Health and Medical Research Council of Australia (1067405 to A.S.Y., G.A.G., and Z.N. and 1037320 to A.S.Y.). A.S.Y. is a Research Fellow of the National Health and Medical Research Council of Australia (1044041). L.C. was funded under the Programme for Research in Third Level Institutions Cycle 5 and cofunded by the European Regional Development Fund. Z.N. is supported by an Australian Research Council Future Fellowship. Optical imaging was performed at the Australian Cancer Research Foundation/Institute for Molecular Bioscience Cancer Biology Imaging Facility, which was established with the generous support of the Australian Cancer Research Foundation.

REFERENCES

- Abreu-Blanco MT, Verboon JM, Liu R, Watts JJ, Parkhurst SM (2012). Drosophila embryos close epithelial wounds using a combination of cellular protrusions and an actomyosin purse string. *J Cell Sci* 125, 5984–5997.
- Aigouy B, Farhadifar R, Staple DB, Sagner A, Roper JC, Julicher F, Eaton S (2010). Cell flow reorients the axis of planar polarity in the wing epithelium of Drosophila. *Cell* 142, 773–786.
- Albert PJ, Schwarz US (2016). Dynamics of cell ensembles on adhesive micropatterns: bridging the gap between single cell spreading and collective cell migration. *PLoS Comput Biol* 12, e1004863.
- Anon E, Serra-Picamal X, Hersen P, Gauthier NC, Sheetz MP, Trepat X, Ladoux B (2012). Cell crawling mediates collective cell migration to close undamaged epithelial gaps. *Proc Natl Acad Sci USA* 109, 10891–10896.
- Bambadekar K, Clement R, Blanc O, Chardes C, Lenne PF (2015). Direct laser manipulation reveals the mechanics of cell contacts in vivo. *Proc Natl Acad Sci USA* 112, 1416–1421.
- Banerjee S, Marchetti MC (2012). Contractile stresses in cohesive cell layers on finite-thickness substrates. *Phys Rev Lett* 109, 108101.
- Banerjee S, Utuje KJ, Marchetti MC (2015). Propagating stress waves during epithelial expansion. *Phys Rev Lett* 114, 228101.
- BD DP, Lopez JH, Schwarz JM, Manning ML (2015). A density-independent rigidity transition in biological tissues. *Nat Phys* 11, 1074–1079.
- Bielmeier C, Alt S, Weichselberger V, La Fortezza M, Harz H, Julicher F, Salbreux G, Classen AK (2016). Interface contractility between differently fated cells drives cell elimination and cyst formation. *Curr Biol* 26, 563–574.
- Borghi N, Sorokina M, Shcherbakova OG, Weis WI, Pruitt BL, Nelson WJ, Dunn AR (2012). E-cadherin is under constitutive actomyosin-generated tension that is increased at cell-cell contacts upon externally applied stretch. *Proc Natl Acad Sci USA* 109, 12568–12573.
- Caballero D, Voituriez R, Riveline D (2014). Protrusion fluctuations direct cell motion. *Biophys J* 107, 34–42.
- Caldwell BJ, Lucas C, Kee AJ, Gaus K, Gunning PW, Hardeman EC, Yap AS, Gomez GA (2014). Tropomyosin isoforms support actomyosin biogenesis to generate contractile tension at the epithelial zonula adherens. *Cytoskeleton (Hoboken)* 71, 663–676.
- Canela-Xandri O, Sagues F, Casademunt J, Buceta J (2011). Dynamics and mechanical stability of the developing dorsoventral organizer of the wing imaginal disc. *PLoS Comput Biol* 7, e1002153.
- Chiou KK, Hufnagel L, Shraiman BI (2012). Mechanical stress inference for two dimensional cell arrays. *PLoS Comput Biol* 8, e1002512.
- Coburn L, Cerone L, Torney C, Couzin ID, Neufeld Z (2013). Tactile interactions lead to coherent motion and enhanced chemotaxis of migrating cells. *Phys Biol* 10, 046002.
- Conway DE, Breckenridge MT, Hinde E, Gratton E, Chen CS, Schwartz MA (2013). Fluid shear stress on endothelial cells modulates mechanical tension across VE-cadherin and PECAM-1. *Curr Biol* 23, 1024–1030.
- Das T, Safferling K, Rausch S, Grabe N, Boehm H, Spatz JP (2015). A molecular mechanotransduction pathway regulates collective migration of epithelial cells. *Nat Cell Biol* 17, 276–287.
- Edwards CM, Schwarz US (2011). Force localization in contracting cell layers. *Phys Rev Lett* 107, 128101.
- Farhadifar R, Roper JC, Aigouy B, Eaton S, Julicher F (2007). The influence of cell mechanics, cell-cell interactions, and proliferation on epithelial packing. *Curr Biol* 17, 2095–2104.
- Farooqui R, Fenteany G (2005). Multiple rows of cells behind an epithelial wound edge extend cryptic lamellipodia to collectively drive cell-sheet movement. *J Cell Sci* 118, 51–63.
- Fernandez-Gonzalez R, Simoes Sde M, Roper JC, Eaton S, Zallen JA (2009). Myosin II dynamics are regulated by tension in intercalating cells. *Dev Cell* 17, 736–743.
- Fletcher AG, Osterfield M, Baker RE, Shvartsman SY (2014). Vertex models of epithelial morphogenesis. *Biophys J* 106, 2291–2304.
- Gomez GA, McLachlan RW, Wu SK, Caldwell BJ, Moussa E, Verma S, Bastiani M, Priya R, Parton RG, Gaus K, et al. (2015). An RPTPalpha/Src family kinase/Rap1 signaling module recruits myosin IIB to support contractile tension at apical E-cadherin junctions. *Mol Biol Cell* 26, 1249–1262.
- Gomez GA, McLachlan RW, Yap AS (2011). Productive tension: force-sensing and homeostasis of cell-cell junctions. *Trends Cell Biol* 21, 499–505.
- Grashoff C, Hoffman BD, Brenner MD, Zhou R, Parsons M, Yang MT, McLean MA, Sligar SG, Chen CS, Ha T, Schwartz MA (2010). Measuring mechanical tension across vinculin reveals regulation of focal adhesion dynamics. *Nature* 466, 263–266.
- Hannezo E, Prost J, Joanny JF (2014). Theory of epithelial sheet morphology in three dimensions. *Proc Natl Acad Sci USA* 111, 27–32.
- Jasaitis A, Estevez M, Heysch J, Ladoux B, Dufour S (2012). E-cadherin-dependent stimulation of traction force at focal adhesions via the Src and PI3K signaling pathways. *Biophys J* 103, 175–184.
- Kabla AJ (2012). Collective cell migration: leadership, invasion and segregation. *J R Soc Interface* 9, 3268–3278.
- Lecuit T, Yap AS (2015). E-cadherin junctions as active mechanical integrators in tissue dynamics. *Nat Cell Biol* 17, 533–539.
- Leerberg JM, Gomez GA, Verma S, Moussa EJ, Wu SK, Priya R, Hoffman BD, Grashoff C, Schwartz MA, Yap AS (2014). Tension-sensitive actin assembly supports contractility at the epithelial zonula adherens. *Curr Biol* 24, 1689–1699.
- Liu Z, Tan JL, Cohen DM, Yang MT, Sniadecki NJ, Ruiz SA, Nelson CM, Chen CS (2010). Mechanical tugging force regulates the size of cell-cell junctions. *Proc Natl Acad Sci USA* 107, 9944–9949.
- Magno R, Grieneisen VA, Maree AF (2015). The biophysical nature of cells: potential cell behaviours revealed by analytical and computational studies of cell surface mechanics. *BMC Biophys* 8, 8.
- Mammoto T, Mammoto A, Ingber DE (2013). Mechanobiology and developmental control. *Annu Rev Cell Dev Biol* 29, 27–61.
- Mao Y, Baum B (2015). Tug of war—the influence of opposing physical forces on epithelial cell morphology. *Dev Biol* 401, 92–102.
- Martiel JL, Leal A, Kurzawa L, Balland M, Wang I, Vignaud T, Tseng Q, Thery M (2015). Measurement of cell traction forces with ImageJ. *Methods Cell Biol* 125, 269–287.
- Martinez-Rico C, Pincet F, Thiery JP, Dufour S (2010). Integrins stimulate E-cadherin-mediated intercellular adhesion by regulating Src-kinase activation and actomyosin contractility. *J Cell Sci* 123, 712–722.
- Maruthamuthu V, Sabass B, Schwarz US, Gardel ML (2011). Cell-ECM traction force modulates endogenous tension at cell-cell contacts. *Proc Natl Acad Sci USA* 108, 4708–4713.
- Mertz AF, Banerjee S, Che Y, German GK, Xu Y, Hyland C, Marchetti MC, Horsley V, Dufresne ER (2012). Scaling of traction forces with the size of cohesive cell colonies. *Phys Rev Lett* 108, 198101.
- Mertz AF, Che Y, Banerjee S, Goldstein JM, Rosowski KA, Revilla SF, Niessen CM, Marchetti MC, Dufresne ER, Horsley V (2013). Cadherin-based intercellular adhesions organize epithelial cell-matrix traction forces. *Proc Natl Acad Sci USA* 110, 842–847.
- Michael M, Meiring JC, Acharya BR, Matthews DR, Verma S, Han SP, Hill MM, Parton RG, Gomez GA, Yap AS (2016). Coronin 1B reorganizes the architecture of F-actin networks for contractility at steady-state and apoptotic adherens junctions. *Dev Cell* 37, 58–71.
- Misra M, Audoly B, Kevrekidis IG, Shvartsman SY (2016). Shape transformations of epithelial shells. *Biophys J* 110, 1670–1678.
- Ng MR, Besser A, Brugge JS, Danuser G (2014). Mapping the dynamics of force transduction at cell-cell junctions of epithelial clusters. *Elife* 3, e03282.
- Nier V, Jain S, Lim CT, Ishihara S, Ladoux B, Marcq P (2016). Inference of internal stress in a cell monolayer. *Biophys J* 110, 1625–1635.
- Noppe AR, Roberts AP, Yap AS, Gomez GA, Neufeld Z (2015). Modelling wound closure in an epithelial cell sheet using the cellular Potts model. *Integr Biol (Camb)* 7, 1253–1264.
- Notbohm J, Banerjee S, Utuje KJ, Gweon B, Jang H, Park Y, Shin J, Butler JP, Fredberg JJ, Marchetti MC (2016). Cellular contraction and polarization drive collective cellular motion. *Biophys J* 110, 2729–2738.

- Park JA, Kim JH, Bi D, Mitchel JA, Qazvini NT, Tantisira K, Park CY, McGill M, Kim SH, Gweon B, et al. (2015). Unjamming and cell shape in the asthmatic airway epithelium. *Nat Mater* 14, 1040–1048.
- Polacheck WJ, Chen CS (2016). Measuring cell-generated forces: a guide to the available tools. *Nat Methods* 13, 415–423.
- Polyakov O, He B, Swan M, Shaevitz JW, Kaschube M, Wieschaus E (2014). Passive mechanical forces control cell-shape change during *Drosophila* ventral furrow formation. *Biophys J* 107, 998–1010.
- Poujade M, Grasland-Mongrain E, Hertzog A, Jouanneau J, Chavrier P, Ladoux B, Buguin A, Silberzan P (2007). Collective migration of an epithelial monolayer in response to a model wound. *Proc Natl Acad Sci USA* 104, 15988–15993.
- Ratheesh A, Gomez GA, Priya R, Verma S, Kovacs EM, Jiang K, Brown NH, Akhmanova A, Stehbens SJ, Yap AS (2012). Centralspindlin and alpha-catenin regulate Rho signalling at the epithelial zonula adherens. *Nat Cell Biol* 14, 818–828.
- Rauzi M, Lenne PF, Lecuit T (2010). Planar polarized actomyosin contractile flows control epithelial junction remodelling. *Nature* 468, 1110–1114.
- Roca-Cusachs P, del Rio A, Puklin-Faucher E, Gauthier NC, Biais N, Sheetz MP (2013). Integrin-dependent force transmission to the extracellular matrix by alpha-actinin triggers adhesion maturation. *Proc Natl Acad Sci USA* 110, E1361–E1370.
- Roycroft A, Mayor R (2016). Molecular basis of contact inhibition of locomotion. *Cell Mol Life Sci* 73, 1119–1130.
- Saez A, Anon E, Ghibaudo M, du Roure O, Di Meglio JM, Hersen P, Silberzan P, Buguin A, Ladoux B (2010). Traction forces exerted by epithelial cell sheets. *J Phys Condens Matter* 22, 194119.
- Scarpa E, Szabo A, Bibonne A, Theveneau E, Parsons M, Mayor R (2015). Cadherin switch during EMT in neural crest cells leads to contact inhibition of locomotion via repolarization of forces. *Dev Cell* 34, 421–434.
- Shewan AM, Maddugoda M, Kraemer A, Stehbens SJ, Verma S, Kovacs EM, Yap AS (2005). Myosin 2 is a key Rho kinase target necessary for the local concentration of E-cadherin at cell-cell contacts. *Mol Biol Cell* 16, 4531–4542.
- Smutny M, Behrndt M, Campinho P, Ruprecht V, Heisenberg CP (2015). UV laser ablation to measure cell and tissue-generated forces in the zebrafish embryo *in vivo* and *ex vivo*. *Methods Mol Biol* 1189, 219–235.
- Smutny M, Cox HL, Leerberg JM, Kovacs EM, Conti MA, Ferguson C, Hamilton NA, Parton RG, Adelstein RS, Yap AS (2010). Myosin II isoforms identify distinct functional modules that support integrity of the epithelial zonula adherens. *Nat Cell Biol* 12, 696–702.
- Staple DB, Farhadifar R, Roper JC, Aigouy B, Eaton S, Julicher F (2010). Mechanics and remodelling of cell packings in epithelia. *Eur Phys J E Soft Matter* 33, 117–127.
- Style RW, Boltynskiy R, German GK, Hyland C, MacMinn CW, Mertz AF, Wilen LA, Xu Y, Dufresne ER (2014). Traction force microscopy in physics and biology. *Soft Matter* 10, 4047–4055.
- Sugimura K, Ishihara S (2013). The mechanical anisotropy in a tissue promotes ordering in hexagonal cell packing. *Development* 140, 4091–4101.
- Tambe DT, Croutelle U, Trepaut X, Park CY, Kim JH, Millet E, Butler JP, Fredberg JJ (2013). Monolayer stress microscopy: limitations, artifacts, and accuracy of recovered intercellular stresses. *PLoS One* 8, e55172.
- Trepaut X, Wasserman MR, Angelini TE, Millet E, Weitz DA, Butler JP, Fredberg JJ (2009). Physical forces during collective cell migration. *Nat Phys* 5, 426–430.
- Weber GF, Bjerke MA, DeSimone DW (2012). A mechanoresponsive cadherin-keratin complex directs polarized protrusive behavior and collective cell migration. *Dev Cell* 22, 104–115.
- Wong S, Guo WH, Wang YL (2014). Fibroblasts probe substrate rigidity with filopodia extensions before occupying an area. *Proc Natl Acad Sci USA* 111, 17176–17181.
- Wu SK, Gomez GA, Michael M, Verma S, Cox HL, Lefevre JG, Parton RG, Hamilton NA, Neufeld Z, Yap AS (2014). Cortical F-actin stabilization generates apical-lateral patterns of junctional contractility that integrate cells into epithelia. *Nat Cell Biol* 16, 167–178.
- Yonemura S, Wada Y, Watanabe T, Nagafuchi A, Shibata M (2010). alpha-Catenin as a tension transducer that induces adherens junction development. *Nat Cell Biol* 12, 533–542.
- Zaritsky A, Welf ES, Tseng YY, Rabadian MA, Serra-Picamal X, Trepaut X, Danuser G (2015). Seeds of locally aligned motion and stress coordinate a collective cell migration. *Biophys J* 109, 2492–2500.
- Zimmermann J, Camley BA, Rappel WJ, Levine H (2016). Contact inhibition of locomotion determines cell-cell and cell-substrate forces in tissues. *Proc Natl Acad Sci USA* 113, 2660–2665.
- Zimmermann J, Hayes RL, Basan M, Onuchic JN, Rappel WJ, Levine H (2014). Intercellular stress reconstitution from traction force data. *Biophys J* 107, 548–554.